Sameep Rajubhai Shah
School of Mechanical Engineering,
Purdue University,
585 Purdue Mall,
West Lafayette, IN 47907
e-mail: shah484@purdue.edu

Luize Scalco de Vasconcelos
School of Mechanical Engineering,
Purdue University,
585 Purdue Mall,
West Lafayette, IN 47907
e-mail: luizevasconcelos@utexas.edu

Kejie Zhao[1]
Fellow ASME
School of Mechanical Engineering,
Purdue University,
585 Purdue Mall,
West Lafayette, IN 47907
e-mail: kjzhao@purdue.edu

Computational Modeling of Electrochemomechanics of High-Capacity Composite Electrodes in Li-Ion Batteries

Mechanical failure and its interference with electrochemistry are a roadblock in deploying high-capacity electrodes for Li-ion batteries. Computational prediction of the electrochemomechanical behavior of high-capacity composite electrodes is a significant challenge because of (i) complex interplay between mechanics and electrochemistry in the form of stress-regulated Li transport and interfacial charge transfer, (ii) thermodynamic solution non-ideality, (iii) nonlinear deformation kinematics and material inelasticity, and (iv) evolving material properties over the state of charge. We develop a computational framework that integrates the electrochemical response of batteries modulated by large deformation, mechanical stresses, and dynamic material properties. We use silicon as a model system and construct a microstructurally resolved porous composite electrode model. The model concerns the effect of large deformation of silicon on charge conduction and electrochemical response of the composite electrode, impact of mechanical stress on Li transport and interfacial charge transfer, and asymmetric charging/discharging kinetics. The study captures the rate-dependent, coupled electrochemomechanical behavior of high-capacity composite electrodes that agrees well with experimental results. [DOI: 10.1115/1.4054759]

Keywords: computational mechanics, silicon composite anode, micromechanics, stress analysis, lithium-ion battery

Introduction

Lithium-ion batteries have dominated the consumer electronics and electric vehicle (EV) market for many years. Still, the need for increased power and energy densities and longer cycle life is unwavering. With the lattice structure and redox kinetics limiting the maximum achievable capacity of intercalation-based active materials, alloying [1–3] and conversion [4] type materials have emerged as alternative high-capacity materials. While conversion electrodes often require a large overpotential to drive the Li reaction, alloying-type electrodes such as silicon, germanium, and tin become the choice for the near-term viable technology due to their high theoretical specific capacity ($\sim 990 - 4000$ mAh g^{-1}), favorable voltage window ($\sim 0.3 - 0.6$ V versus Li/Li^+), abundant raw material availability, relatively low cost, and pre-existing material processing techniques [2,4–7]. However, due to the nature of alloying reactions, the electrodes inherently undergo significant volume changes (up to ~300%) upon (de)lithiation [8]. This extreme deformation combined with large diffusion-induced stresses often leads to fracture and pulverization of the active material, resulting in loss of electrical contact and subsequent capacity fade [6,9–12]. Moreover, the large volume change causes continuous fracture and re-formation of the solid electrolyte interphase (SEI) layer, and the dynamic thickening of the SEI layer over cycles leads to continuous depletion of Li ions [9–12]. Additionally, pulverization of active materials provides fresh surfaces for the formation of new SEI. Cyclic expansion–contraction and SEI pore-filling have a combined effect of impeding ion-conducting pathways, adversely affecting electrochemical transport within the electrode and leading to drastic capacity fade [13]. While the qualitative consequence of volume expansion mentioned above is well recognized, the direct and quantitative link between deformation and electrochemical performance of the cell is less studied. Pietsch et al. [14] found a direct correlation between the volume expansion and porosity reduction, resulting in increased tortuosity in graphite anodes. They also reported a 7.6% drop in porosity for a silicon composite electrode due to electrode expansion during lithiation. Dhillon et al. [15] used a 1D electrochemical model coupled with a particle growth model to study the heterogeneous evolution of porosity in silicon composite electrodes at different charging rates. Li trapping within active particles is another issue associated with the irreversible capacity loss in high-capacity electrodes [16,17]. Recent studies suggest that Li trapping is a diffusion-controlled phenomenon [18,19]. de Vasconcelos et al. [20] presented a theory accounting for the asymmetric diffusion kinetics during lithiation and delithiation that explains an underlying mechanism of Li trapping in silicon particles.

Multiple technologies and solutions have been developed to combat the mechanical obstacles in high-capacity electrodes, leading to significant improvement in the cell stability in the past decade. Nanostructured materials are capable of accommodating large volume changes without fracture. Therefore, nanostructured electrodes in the form of nanowires [1,21,22], nanoparticles [23,24], and nanotubes [25,26] have shown improved cyclic life. Other composite designs, including yolk-shell Si/C and Sn/C composite electrodes [27,28], silicon backboned graphene hybrid structures [29], Si/Ge-carbon nanotube structures [30,31], have presented novel ways to actualize high-capacity anodes. However, nanostructured electrodes have not yet fully realized their potential due to lower tap density, lower Coulombic efficiency, and complex manufacturing processes. Alternatively, grafting small amounts of active material ($5 - 20\%$ wt.) with carbon is a viable intermediate step in achieving higher capacities than conventional graphite anodes [3,32–39]. These composite electrodes have shown good capacity retention over elongated cycles. Due to their

[1]Corresponding author.

Contributed by the Applied Mechanics Division of ASME for publication in the Journal of Applied Mechanics. Manuscript received April 25, 2022; final manuscript received June 4, 2022; published online June 27, 2022. Assoc. Editor: Haleh Ardebili.

relative ease in manufacturing, many such composite electrodes are currently commercially available for EV and portable electronics.

On the computational side, modeling high-capacity composite electrodes presents a unique challenge due to the complex electrochemomechanical interactions along with material and geometric nonlinearities. The large volumetric changes upon (de)lithiation make it necessary to formulate the governing equations using finite deformation kinematics. Experimental observations of the rate-dependent plastic response of silicon during (de)lithiation call for a viscoplastic constitutive model to describe the material's nonlinearity [40]. Furthermore, the large concentration range in high-capacity materials generally implies that the enthalpy of mixing is a significant term, and the free energy change due to the interactions between the Li – host atoms and Li – Li atoms must be included in the form of the thermodynamic activity coefficient in the Larché-Cahn chemical potential expression [41,42]. Often in modeling mass transport, the activity coefficient is embedded in the diffusivity coefficient instead of being explicitly modeled; however, de Vasconcelos et al. [20] demonstrated that this simplification is not appropriate when modeling stress-regulated diffusion; otherwise, it leads to an artificial imbalance between the chemical and mechanical driving forces for diffusion. Sethuraman et al. [43] experimentally observed the coupling between mechanical stress and interfacial electrochemical reactions in an amorphous silicon thin film. They reported a significant change in the open-circuit potential with changing stress levels at a constant state of charge (SOC). Bower et al. [44] developed a finite strain model with a thermodynamic foundation that presented a generalized Nernst equation for the equilibrium potential, which included the influence of the change in free energy due to the presence of mechanical stresses. While the open-circuit potential directly affects the interfacial charge transfer (ICT), Lu et al. [45] and Ganser et al. [46] presented alternate but equivalent modifications to the phenomenological Butler–Volmer equation to model the stress modulated ICT. Xu et al. [47] and Liu et al. [48] reported that the stress effect on ICT in lithium nickel manganese cobalt oxide (NMC) cathodes is insignificant at moderate charging rates. Using silicon as a model system, we strive to tackle these challenges by developing a computational framework that integrates the electrochemical response of high-capacity composite electrodes modulated by the large deformation and mechanical stresses.

With interest in silicon anodes picking up in the past few years, there have been numerous computational studies on silicon composite electrodes. Building on the continuum model developed by Bower et al. [44], Bucci et al. [42] presented a coupled electrochemomechanical model for silicon thin-film electrodes. The model included accurate stress coupling, rate-dependent plasticity, SOC-dependent mechanical properties, and non-ideal mixing thermodynamics. de Vasconcelos et al. [20] expanded this model to include the concentration dependence of the diffusion coefficient, which leads to asymmetric diffusion kinetics and Li trapping that is related to the electrochemical performance. Various studies explicitly define active particles and the surrounding porous matrix to develop microstructure resolved models for NMC [47–49] and graphite/$LiCoO_2$ (LCO) [50]. The models by Trembacki et al. [51–53], Srivastava et al. [54], and Ferraro et al. [55] explicitly define the three phases, active material, carbon-binder domain (CBD), and pores, in a porous NMC electrode. It enables reproducing the evolution of the porosity and tortuosity of the composite electrode and quantifying the impact of deformation and external compression on the transport of Li ions in the liquid electrolyte. Wang et al. [56] presented a microstructure resolved model of a silicon electrode, explicitly modeling the pore phase and active material, albeit using a simplified rod geometry and excluding CBD altogether. Gao et al. [57] and Liu et al. [58] presented multi-scale models for commercial silicon composite electrodes. The former studied the effect of silicon content, mechanical constraint, and charging rate on the performance of a Si – C composite electrode paired with an LCO cathode in full cell configuration. The latter coupled electrochemistry at the particle scale with homogenized mechanics of the jellyroll at the cell scale. The resulting model helps guide cell design to mitigate the failure of the composite electrode. All these specialized models serve to study specific aspects of silicon composite electrodes.

Here, we present a fully coupled electrochemomechanical computational framework that integrates (i) finite strain kinematics, (ii) the rate-dependent viscoplastic constitutive behavior, (iii) chemomechanical stress coupling, (iv) solution non-ideality, (v) the stress effect on ICT, and (vi) concentration-dependent diffusion coefficient and material properties. We construct a microstructurally resolved porous silicon composite model from previous backscatter scanning electron microscopy (SEM) images obtained from the work of Müller et al. [9]. Figure 1(*a*) shows a schematic of a porous silicon electrode coupled with a Li counter electrode in a half-cell configuration. Figure 1(*b*) shows the enlarged cross section of a silicon particle in the pristine and lithiated (deformed) configurations. We use the computational framework to capture the rate-dependence of the electrochemomechanical behavior of the silicon electrode and assess the influence of the thermodynamic non-ideality on the solution kinetics and the resulting modulation of the chemomechanical interaction. The microstructurally resolved model provides the ability to model the evolution of porosity and tortuosity and to quantify the impact of deformation (Fig. 1(*b*) (i)) on the transport of Li ions in the liquid electrolyte. The impact of mechanical stress on ICT reactions on silicon—electrolyte/CBD interface (Fig. 1(*b*) (ii)) is also studied. We further enhance the model by including concentration-dependent mechanical properties and the nonlinear asymmetric kinetics of Li diffusion (Fig. 1(*b*) (iii)). We study the resulting capacity loss after a complete charge–discharge cycle for a range of diffusion coefficients.

Theory and Computational Modeling

Porous composite electrodes generally consist of three components (Fig. 1(*a*)): active particles, CBD, and liquid electrolyte-filled pore phase. Lithiation of silicon particles involves the transport of Li ions from the lithium metal counter electrode to the active particle through the liquid electrolyte, passing the separator and then through the pore network. Electrons are transported from lithium metal to the electrode current collector through the external circuit. The carbon-binder network forms the conducting pathways for the electrons from the current collector to the active particles. Electrons and Li ions combine at the surface of the active particles to form neutral Li, which then diffuses within the silicon active particles. Electrochemical transport processes in porous electrodes are well described by the pioneering work by Newman et al. [59,60]. Finite deformation kinematics and mechanics theories describe Li insertion-induced volume change and the resulting stress fields in the active particles and the conducting matrix. Instead of treating the porous electrode as a homogenous continuous medium, we model each of the three phases explicitly based on an SEM image of a pristine silicon composite electrode presented by Müller et al. [9]. The two-dimensional axisymmetric geometry generated from the image is shown in Fig. 2(*a*) (inset). We summarize the governing equations and boundary conditions used for the fully coupled electrochemomechanical model in this section.

Deformation and Stresses. The coordinate of each spatial point in the reference undeformed configuration is defined as the material coordinate $\mathbf{X}$. As the material deforms, the resulting displacement vector is denoted as $\mathbf{u}(\mathbf{X}, t)$. The resulting coordinate of each material point in the deformed or current configuration defines the spatial coordinate $\mathbf{x}$, given by

$$\mathbf{x}(\mathbf{X}, t) = \mathbf{X} + \mathbf{u}(\mathbf{X}, t) \tag{1}$$

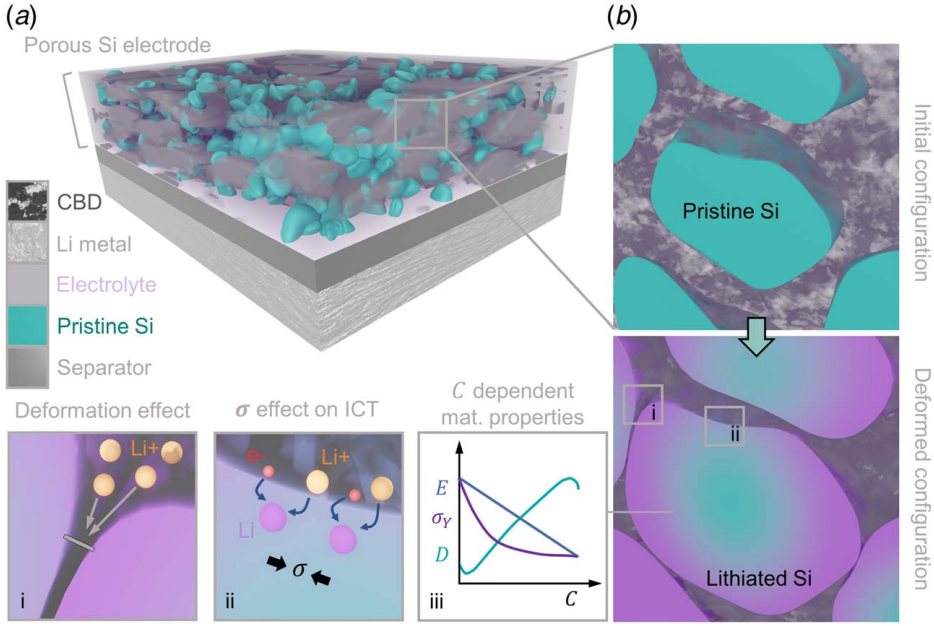

Fig. 1 Schematic representation of the prime concepts of this study: (*a*) schematic of a half-cell consisting of a porous silicon electrode coupled with Li metal, separated by a separator and (*b*) magnified view of silicon particles and the surrounding CBD, and pore phase in the pristine state (initial configuration) and lithiated state (deformed configuration). Further magnified schematics showing (i) the effect of deformation on Li ion transport, (ii) stress effect on ICT, and (iii) SOC-dependent material properties including elastic modulus, yield strength, and diffusion coefficient.

The material deformation gradient tensor $\mathbf{F}$ is defined as

$$\mathbf{F} = \frac{\partial \mathbf{x}}{\partial \mathbf{X}} = \nabla \mathbf{u} + \mathbf{I} \tag{2}$$

The deformation gradient follows multiplicative decomposition

$$\mathbf{F} = \mathbf{F}_{\text{el}}\mathbf{F}_{\text{Li}}\mathbf{F}_{\text{vp}} \tag{3}$$

where $\mathbf{F}_{\text{el}}$ represents elastic deformation, $\mathbf{F}_{\text{Li}}$ represents the stress-free deformation due to lithiation and delithiation, and $\mathbf{F}_{\text{vp}}$ represents the inelastic viscoplastic deformation. The change in volume with respect to the initial volume is given by the determinant of the deformation gradient $\mathbf{F}$

$$\frac{\partial V}{\partial V_0} = \det(\mathbf{F}) = J \tag{4}$$

The change in volume due to lithiation and delithiation, J_{Li} is solely dependent on the change in Li concentration $C(\mathbf{X}, t)$

$$J_{\text{Li}} = \det(\mathbf{F}_{\text{Li}}) = (1 + \Omega C) \tag{5}$$

where Ω is the partial molar volume of Li in silicon. From Eq. (5), assuming isotropic expansion in all directions, the relation between the lithiation and delithiation-induced deformation gradient $\mathbf{F}_{\text{Li}}$ can be obtained

$$\mathbf{F}_{\text{Li}} = (1 + \Omega C)^{\frac{1}{3}}\mathbf{I} \tag{6}$$

where $\mathbf{I}$ is the identity tensor. The first Piola-Kirchhoff (PK) stress tensor $\mathbf{P}$ satisfies mechanical equilibrium

$$\nabla \cdot \mathbf{P} + \mathbf{B}_{\text{v}} = 0 \tag{7}$$

Here, the del operator ∇ is with reference to the undeformed configuration. $\mathbf{B}_v$ is the volume force. The first PK stress $\mathbf{P}$ is related to the second PK stress $\mathbf{S}$ as

$$\mathbf{P} = \mathbf{FS} \tag{8}$$

The commonly used symmetric Cauchy stress tensor $\boldsymbol{\sigma}$ is related to second PK stress as

$$\boldsymbol{\sigma} = J^{-1}\mathbf{FSF}^{\text{T}} \tag{9}$$

The elastic second PK stress is related to the elastic Green–Lagrange strain tensor $\mathbf{E}_{\text{el}}$ by

$$\mathbf{S}_{\text{el}} = J_{\text{el}}\mathbf{F}_{\text{el}}^{-1}\boldsymbol{\sigma}\mathbf{F}_{\text{el}}^{-\text{T}} = \mathbb{C} : \mathbf{E}_{\text{el}} \tag{10}$$

where $\mathbb{C}$ is the elastic stiffness tensor. The Green–Lagrange strain can be obtained from the elastic right Cauchy–Green deformation tensor $\mathbf{C}_{\text{el}} = \mathbf{F}_{\text{el}}^{\text{T}}\mathbf{F}_{\text{el}}$

$$\mathbf{E}_{\text{el}} = \frac{1}{2}(\mathbf{C}_{\text{el}} - \mathbf{I}) = \frac{1}{2}(\mathbf{F}_{\text{el}}^{\text{T}}\mathbf{F}_{\text{el}} - \mathbf{I}) \tag{11}$$

The viscoplastic constitutive law relates the rate change of inelastic strain $\boldsymbol{\varepsilon}_{vp}$ with the stress as

$$\frac{\partial \boldsymbol{\varepsilon}_{vp}}{\partial t} = \begin{cases} \mathbf{0} & \sigma_e \le \sigma_Y \\ A\left(\dfrac{\sigma_e - \sigma_Y}{\sigma_Y}\right)^n \mathbf{D} & \sigma_e > \sigma_Y \end{cases} \tag{12}$$

where A and n are material constants, σ_e is the equivalent or von-Mises stress, σ_Y is the yield strength, and $\mathbf{D}$ is the deviatoric tensor coaxial to the stress tensor. The inactive material surrounding silicon is considered a Neo-Hookean hyperelastic material that follows a nonlinear relationship between stress and strain. The elastic strain energy density W is a function of the first invariant of the elastic right Cauchy–Green deformation tensor $I_1(\mathbf{C}_{\text{el}})$ and the elastic volume ratio J_{el}

$$W = \frac{1}{2}\mu_{\text{h}}(I_1 - 3) - \mu_{\text{h}}\ln(J_{\text{el}}) + \frac{1}{2}\lambda_h[\ln(J_{\text{el}})]^2 \tag{13}$$

where μ_{h} and λ_h are the Lamé parameters. The second PK stress can then be evaluated as

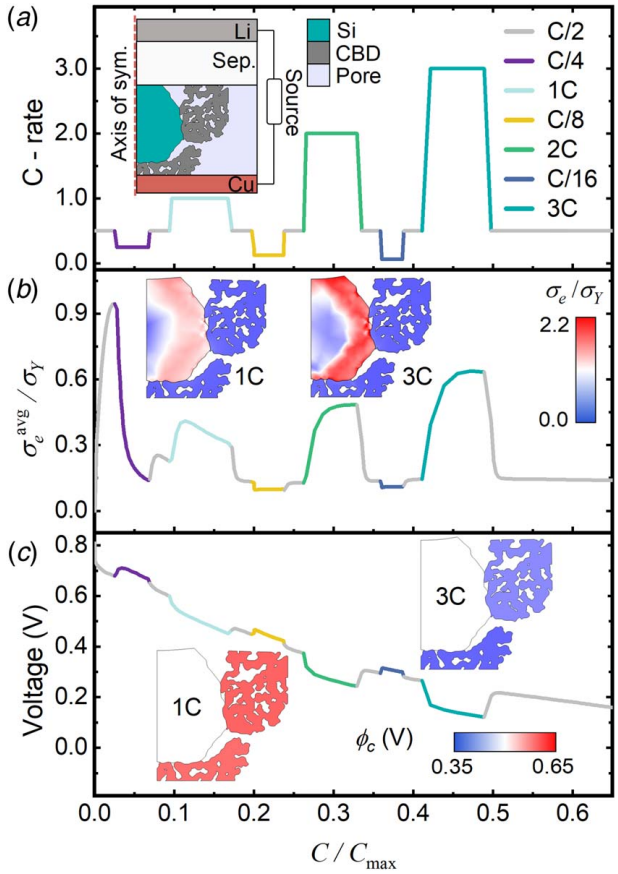

Fig. 2 Rate-dependent mechanical and electrochemical behaviors of a silicon composite electrode during lithiation at different charging rates: (*a*) Variation of the C-rate from C/16 to 3C. Inset shows the axisymmetric half-cell model with the microstructure of the silicon electrode determined from experimental SEM images [9], (*b*) Rate-dependent stress response in the electrode. Inset figures show contour plots of the normalized equivalent stress at the charging state $C/C_{max} = 0.05$ for 1C and 3C, and (*c*) Rate-dependent voltage response of the electrode. Inset shows contour plots of ϕ_c in the conductive matrix at $C/C_{max} = 0.05$ for 1C and 3C.

$$\mathbf{S} = 2\frac{\partial W}{\partial \mathbf{C}} \tag{14}$$

where $\mathbf{C}$ is the right Cauchy–Green deformation tensor. The geometry is assumed to be axisymmetric about the axis $r = 0$ as shown in the inset of Fig. 2(*a*). Radial displacement on $r = R_0$, as well as the axial displacements at the current collector ($z = 0$) and Li metal ($z = L$) surfaces, is assumed fixed. Using unit normal vector pointing from the porous electrode to the current collector $\mathbf{n}_{ac}$, from the separator to Li metal $\mathbf{n}_{Li}$, and from $r = R_0$ toward the outside of the model $\mathbf{n}_s$, the boundary conditions for the mechanical deformation are written as follows:

$$\begin{aligned} &\mathbf{u} \cdot \mathbf{n}_s = 0 \text{ at } r = R_0; \\ &\mathbf{u} \cdot \mathbf{n}_{ac} = 0 \text{ at } z = 0 \text{ and } \mathbf{u} \cdot \mathbf{n}_{Li} = 0 \text{ at } z = L \end{aligned} \tag{15}$$

Electrochemical Transport. Ohm's law governs the conduction of electrons in the conducting matrix. The electric current density $\mathbf{i}_c$ in the carbon-binder matrix is related to the matrix potential ϕ_c by

$$\mathbf{i}_c = -K_c \nabla \phi_c \tag{16}$$

where K_c is the electrical conductivity of the carbon-binder matrix.

For the conservation of mass within the electrolyte, the accumulation of Li ions must be equal to the net input (assuming no generation of Li ions within the electrolyte)

$$\frac{\partial C_l}{\partial t} + \nabla \cdot \mathbf{J}_l = 0 \tag{17}$$

where C_l is the concentration of Li ions in the electrolyte and $\mathbf{J}_l$ is the flux of Li ions. The movement of the charged Li ions in the liquid electrolyte is due to diffusion in the presence of a concentration gradient and migration in an electric field. Assuming the bulk velocity of the liquid electrolyte is 0, we obtain the following relation for the Li ion flux $\mathbf{J}_l$

$$\mathbf{J}_l = -D_l \nabla C_l + \frac{\mathbf{i}_l t_+}{F} \tag{18}$$

where D_l is the diffusivity of Li ions in the electrolyte, t_+ is the transference number of the cation, and F is Faraday's constant. Accounting for Li ion concentration variation, the electrolyte current density $\mathbf{i}_l$ is defined as [59,60]

$$\mathbf{i}_l = (-K_l \nabla \phi_l) + \frac{2K_l RT}{F}\left(1 + \frac{\partial \ln f}{\partial \ln C_l}\right)(1 - t_+)\ \nabla \ln C_l \tag{19}$$

where K_l is the electrolyte ionic conductivity, ϕ_l is the electrolyte potential, R is the universal gas constant, T is the absolute temperature, and f is the mean activity of the electrolyte.

Electric charge conservation requires that $\mathbf{i}_c$ and $\mathbf{i}_l$ are free of divergence

$$\nabla \cdot \mathbf{i}_c = 0 \tag{20}$$

$$\nabla \cdot \mathbf{i}_l = 0 \tag{21}$$

Defining the additional unit normal vector $\mathbf{n}_{as}$ pointing from the porous electrode to the separator, the externally applied current density i_{app}, and l the total height of the porous electrode, the electrical boundary conditions are described as follows,

$$\begin{aligned} &\mathbf{i}_l \cdot \mathbf{n}_s = 0 \ at\ r = R_0; \\ &\mathbf{i}_c \cdot \mathbf{n}_s = 0 \ at\ r = R_0; \\ &\mathbf{i}_l \cdot \mathbf{n}_{ac} = 0 \ at\ z = 0; \\ &\mathbf{i}_c \cdot \mathbf{n}_{ac} = -i_{app} \ at\ z = 0; \\ &\mathbf{i}_l \cdot \mathbf{n}_{Li} = i_{app} \ at\ z = L; \\ &\mathbf{i}_c \cdot \mathbf{n}_{as} = 0 \ at\ z = l; \\ &\phi_c = 0 \ at\ z = L; \\ &\mathbf{J}_l \cdot \mathbf{n}_s = 0 \ at\ r = R_0; \\ &\mathbf{J}_l \cdot \mathbf{n}_{ac} = 0 \ at\ z = 0; \\ &\mathbf{J}_l \cdot \mathbf{n}_{Li} = \frac{i_{app}}{F} \ at\ z = L \end{aligned} \tag{22}$$

Interfacial Charge Transfer. Li ions in the electrolyte at the electrolyte–silicon interface combine with electrons e^- conducted by CBD to form neutral Li, which is deposited into silicon. The reverse reaction of Li dissociation co-occurs, and this process is defined by the unimolecular reversible reaction $Li^+ + e^- \rightleftharpoons Li$ occurring at the active particle interface. Assuming an ample supply of the reacting species at the interface, the net rate of the ICT reaction is given by the Butler–Volmer equation [60,61]

$$i_{BV} = i_0\left(\exp\left(\frac{\alpha_a F\eta}{RT}\right) - \exp\left(-\frac{\alpha_c F\eta}{RT}\right)\right) \tag{23}$$

where i_{BV} is the local ICT current density, α_a and α_c are the anodic and cathodic transfer coefficients, respectively, i_0 is the exchange current density, and η is the surface overpotential given by

$$\eta = \phi_c - \phi_l - E_{eq} - \frac{\Omega\sigma_m}{F} \tag{24}$$

where E_{eq} is the open-circuit potential and $\sigma_m = tr(\boldsymbol{\sigma})/3$ is the hydrostatic stress in silicon. The last term in Eq. (24) accounts for the stress effect on ICT reactions based on the work of Lu et al. [45]. The exchange current density i_0 in Eq. (23) represents the rate of formation and dissociation of Li at a state of dynamic equilibrium at the interface and is defined as [61]

$$i_0 = F(k_c)^{\alpha_a}(k_a)^{\alpha_c}(C_{\max} - C)^{\alpha_a}(C)^{\alpha_c}\left(\frac{C_l}{C_{l\_ref}}\right)^{\alpha_a} \tag{25}$$

where k_c and k_a are the rate constants of the cathodic and anodic reactions, respectively, $C_{\max}$ is the maximum theoretical concentration of Li in silicon, and C_{l_ref} is the reference Li^+ concentration in the electrolyte.

At the silicon–electrolyte and silicon–CBD interfaces, we have

$$\begin{aligned} \mathbf{i}_{\mathrm{l}} \cdot \mathbf{n}_{\mathrm{l}} &= -i_{BV}; \\ \mathbf{i}_{\mathrm{c}} \cdot \mathbf{n}_{\mathrm{c}} &= i_{BV} \end{aligned} \tag{26}$$

where $\mathbf{n}_{\mathrm{l}}$ is the unit normal vector pointing from the electrolyte phase to silicon and $\mathbf{n}_{\mathrm{c}}$ is the unit normal vector from CBD to silicon.

Lithium Diffusion Kinetics. Neutral Li forms at the active material surface through interfacial reactions and diffuses into the bulk of silicon. Chemical potential μ is the thermodynamic driving force for diffusion. Mechanical stress in the host alters the free energy ensuing in a modification of the chemical potential and, therefore, directly influences the diffusion process. This chemomechanical coupling is modeled by including the stress effect in the expression of chemical potential [42,62]

$$\mu = \mu_0 + RT\ln\left(\frac{\gamma C}{C_{\max} - C}\right) - \Omega\sigma_m \tag{27}$$

where μ_0 is the reference potential, and γ is known as the activity coefficient accounting for the thermodynamic non-ideality. Mass conservation requires

$$\frac{\partial C}{\partial t} + \nabla \cdot \mathbf{J} = 0 \tag{28}$$

Following Fickian diffusion, Li flux in the deformed configuration $\mathbf{j}$ is given by

$$\mathbf{j} = \frac{cD}{RT}\nabla_{\mathbf{x}}\mu \tag{29}$$

where $c(\mathbf{x}, t)$ is the concentration of Li in the deformed configuration, D is the diffusion coefficient, and $\nabla_{\mathbf{x}}(\,)$ is the gradient operator in the deformed configuration. Nanson formula provides the standard relationship between differential area da with normal $\mathbf{n}_0$ in the deformed state and the differential area dA with normal $\mathbf{N}_0$ in the reference state

$$\mathbf{F}^{\mathrm{T}}\ \mathbf{n}_0 da = \det(\mathbf{F})\mathbf{N}_0 dA \tag{30}$$

As the flux of Li is independent of the description system, we have

$$\mathbf{j} \cdot \mathbf{n}_0 da = \mathbf{J} \cdot \mathbf{N}_0 dA \tag{31}$$

Combining the Nanson formula (Eq. (30)) with Eq. (31), we obtain the relation between Li flux in deformed and reference configuration

$$\mathbf{j} = \frac{\mathbf{F}}{\det(\mathbf{F})}\mathbf{J} \tag{32}$$

Li concentration in the deformed and reference configurations are related by

$$c = \frac{C}{\det(\mathbf{F})} \tag{33}$$

Using the chain rule for partial derivatives, the relation between the gradient operator in the reference configuration $\nabla(\,)$ and the deformed configuration $\nabla_{\mathbf{x}}(\,)$ is obtained

$$\nabla_{\mathbf{x}}(\,) = \mathbf{F}^{-\mathrm{T}}\nabla(\,) \tag{34}$$

Combining Eqs. (29)–(34), the relationship between Li flux and chemical potential in the reference configuration is obtained

$$\mathbf{J} = -\frac{CD}{RT}\mathbf{F}^{-1}\mathbf{F}^{-\mathrm{T}}\nabla\mu \tag{35}$$

where the chemical potential μ takes the form described in Eq. (27). The weak formulation for mass transport is derived to input into COMSOL MULTIPHYSICS with chemical potential μ as the field variable as follows:

$$\int_\Omega \left(\frac{\partial C}{\partial t} + \nabla \cdot \mathbf{J}\right) w\mathrm{d}\Omega = 0 \tag{36}$$

where w is an arbitrary test function. Integrating the above integral by parts, we obtain

$$\int_\Omega \frac{\partial C}{\partial t} w\mathrm{d}\Omega\ - \int_\Omega \mathbf{J} \cdot \nabla w\mathrm{d}\Omega\ + \int_\Gamma (\mathbf{J} \cdot \mathbf{N}_0) w\mathrm{d}\Gamma = 0 \tag{37}$$

where $\mathbf{J} \cdot \mathbf{N}_0 = J_0$ is the nominal Li influx into the active material.

At the interface, the Li flux is related to the Butler–Volmer current density as

$$\mathbf{J} \cdot \mathbf{n}_{\mathrm{l}} = -\frac{i_{BV}}{F} \tag{38}$$

Results and Discussion

Rate-Dependent Electrochemical and Mechanical Behaviors. Considering the drastic volumetric changes of silicon upon Li insertion and extraction, the mechanical response of silicon during electrochemical cycles is mostly inelastic. Prior observations on strong rate dependence and stress relaxation in silicon motivated the development of viscoplastic constitutive laws [40,42,44,63–65]. We adopt the constitutive relation of a viscoplastic power law as shown in Eq. (12) for the silicon particle. To unravel the rate dependence of stresses in the active particle, silicon is lithiated at the charging rates of C/4, 1C, C/8, 2C, C/16, and 3C, alternating with a rate of C/2 in between as shown in Fig. 2(*a*). Here, the charging rate is expressed as fractions or multiples of 1C, which represents that the provided current density would fully lithiate the active material nominally in one hour. The x-axis in Fig. 2 is the average Li concentration in the silicon particle, C, normalized by the theoretical maximum concentration, $C_{\max}$. Figure 2(*b*) shows the variation of the average equivalent or von-Mises stress in the active particle, σ_e^{avg} (normalized by the yield stress σ_Y) with varying charging rates. The initial Li insertion and viscoplasticity of silicon lead to a rapid rise in the average equivalent stress. The stress then reduces to a much lower value because the slow charging rate of C/4 induces lower mismatch strains within the particle. The stress then increases steadily for higher charging rates and drops for lower rates. This mechanical response is a clear indication of rate-sensitive inelastic deformation of silicon. The inset images in Fig. 2(*b*) show the distribution of the equivalent stress within the active particle at the same average concentration of $C/C_{\max} = 0.05$ for two separate simulations of lithiation at 1C and 3C. The magnitude of stresses is much higher at both the surface and interior of the particle for the charging rate of 3C in comparison with that of 1C. Figure 2(*c*) shows the rate dependence of the voltage response of the cell. As expected, higher charging rates lead to a rapid drop in the voltage, while slower charging allows for retention at a higher voltage. The inset of Fig. 2(*c*) shows the distribution of the

potential ϕ_c in the conductive matrix for 1C and 3C charging rates. At the same average concentration of $C/C_{max} = 0.05$, ϕ_c is considerably lower for 3C charging rate when compared to 1C because of the consumption of the overpotential to drive Li insertion at a higher rate. These results depict the strong rate sensitivity of the mechanical and electrochemical behaviors of the silicon electrode, which agrees well with the experimental observation reported by Pharr et al. [40] (see Figs. S1(*a*) and S1(*b*) available in the Supplemental Materials on the ASME Digital Collection).

Influence of Thermodynamic Non-ideality. Molecular and ionic interactions of Li inserted into silicon lead to the excess free energy of the system [41]. While in ideal solutions this excess free energy can be neglected, it is significant for Si − Li because of the large capacity of Li absorption in the silicon lattice [66]. We account for this deviation from ideality by using the thermodynamic activity coefficient γ in the formulation of the chemical potential, as shown in Eq. (27). To gauge the influence of the thermodynamic non-ideality on the electrochemical response and on the stress-diffusion coupling, we perform independent charge–discharge modeling of ideal ($\gamma = 1$) and non-ideal ($\gamma = \gamma(C)$) solutions for one complete cycle at 1C, both with and without considering the stress effect on diffusion. In Fig. 3, we plot the half-cell potential against the normalized concentration C/C_{max}. There is a significant difference in the voltage profiles of ideal and non-ideal systems when the stress effect is included (solid lines in Fig. 3). The non-ideal system achieves a much higher lithiation capacity with a slightly higher residual trapped Li at the end of discharge. Comparing the ideal solutions (teal-colored, open circle lines), a considerable difference is shown between the stress-regulated diffusion and uncoupled diffusion. Overall, mechanical stresses tend to homogenize the concentration gradient of Li within the particle due to the mechanical driving force in the diffusion potential, leading to a larger lithiation capacity and a lower residual Li content. In comparison with the ideal solutions, the difference between the coupled and uncoupled diffusion in the non-ideal cases (purple, open triangle lines) is much smaller, especially during Li insertion, indicating the modulation of the thermodynamic activity coefficient on the chemomechanical interactions. Moreover, aside from the dominating effect of thermodynamic non-ideality, mechanical stress tends to retard lithiation in the non-ideal case and allows a lower amount of trapped Li at the end of delithiation (purple, open triangle lines). This effect arises due to tensile stresses occurring close to the particle surface (see Fig. S2 available in the Supplemental Materials on the ASME Digital Collection), due to the bonding between the active particle and surrounding matrix and separator (further elaborated in the next section). Overall, the assessment of the relative impact of the thermodynamic non-ideality versus mechanical stresses on Li transport is in good agreement with the results presented by de Vasconcelos et al. [20].

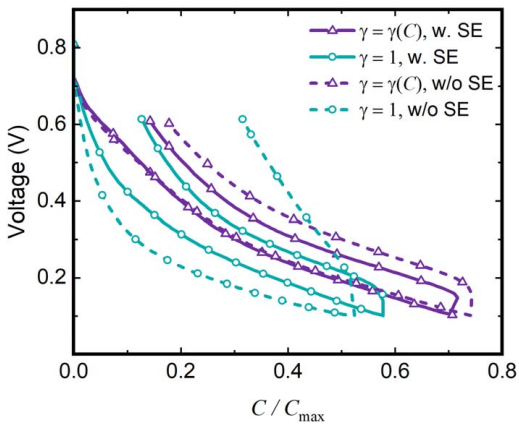

Fig. 3 Effects of thermodynamic non-ideality and mechanical stresses on voltage response of the cell

Stress Effect on Interfacial Charge Transfer. The Butler–Volmer equation describing the charge transfer process at the surface of silicon is modified to include the influence of surface stresses in the active material (Eqs. (23) and (24)). To evaluate the impact of stress on the interfacial reaction, we compare the average interfacial overpotential with the stress-biased voltage $\Omega\sigma_m/F$ in Figs. 4(*a*) and 4(*b*) for a complete lithiation–delithiation cycle at 1C and 3C rates, respectively. Here t is the charging/discharging time, and τ is the theoretical time required to reach the full capacity at a given C-rate ($\tau = 3600$ s for 1C). A negative overpotential indicates a higher rate of the cathodic reaction than the anodic reaction at the interface resulting in a net lithiation effect. The results show that the stress contribution to the overpotential is on the same order of magnitude of the overall overpotential throughout the charging–discharge cycle for both 1C and 3C. Note that $\Omega\sigma_m/F$ approaches 0 and becomes positive (tensile stress) during lithiation at the two charging rates. This unusual behavior arises due to the large tensile stresses at the region where the CBD network and separator contact the active particle (see the stress profiles in Fig. S2 available in the Supplemental Materials on the ASME Digital Collection.). In large-sized composite electrodes, the surface stress likely remains compressive in nature as the silicon–CBD and silicon–separator interfaces cannot withstand such high tensile stresses, and otherwise, it would result in delamination. During lithiation, an active particle in a free-standing configuration experiences compressive stresses on the surface and tensile stresses in the interior due to the diffusion-induced mismatch strain. The compressive stress reduces the magnitude of the overpotential and impedes Li insertion into the silicon particle which results in a lower deliverable capacity. This is a competing effect compared to the stress-mediated diffusion in which a compressive stress on the particle surface promotes diffusion into the bulk and leads to a greater insertion capacity. Figures 4(*c*) and 4(*d*) present the resulting influence on the voltage response of the cell. The voltage curves for a charge–discharge cycle, with and without the stress-biased voltage $\Omega\sigma_m/F$ included in η, are plotted against the normalized time t/τ. For both 1C and 3C charging rates, we see a more significant voltage drop for charging with the stress effect due to the attribution of compressive stresses at the surface at the initial stage of charging. As the particle expands and the surface stresses become tensile at specific locations (as explained before), positive $\Omega\sigma_m/F$ promotes Li insertion which increases the voltage and the deliverable capacity compared to the results without considering the stress effect. This behavior would not occur in the presence of particle delamination, and the particle would have a lower capacity due to the compressive stress-related retardation of charge transfer. Upon delithiation, $\Omega\sigma_m/F$ remains positive, minimizing the overpotential and continually impeding Li extraction, which results in more trapped Li within the active particle at the end of delithiation. While some studies have found that the stress influence on the overpotential is negligible (e.g., NMC [47,48]), the scenario of silicon is different. These results are in line with the theory presented by Sethuraman et al. [43] and Bower et al. [44], which states that due to the electric potential–stress coupling, mechanical energy dissipation results in the loss of useful electrical energy in the cell. As silicon has much larger energy dissipation than NMC due to the inelastic deformation, the influence of stress on the electrochemical performance is, therefore, more significant.

Effect of Deformation on Electrochemical Transport. The extreme volume change of silicon upon Li intake has a striking impact on the electrochemical transport properties of the cell. Figure 5(*a*) plots the percentage volume expansion of the silicon particle during lithiation at 1C on the primary y-axis (left) and the resulting change in porosity and tortuosity of the composite

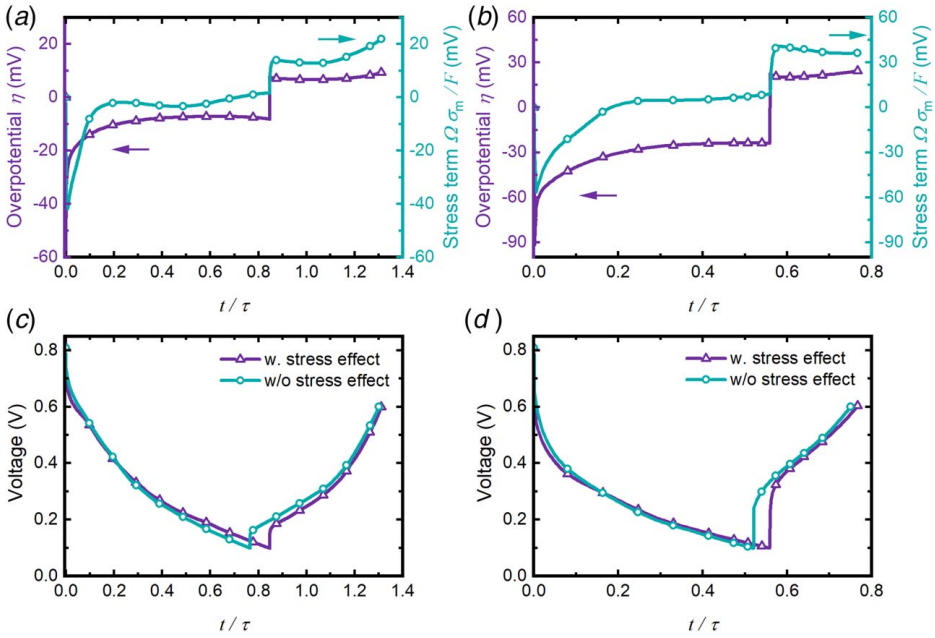

Fig. 4 Influence of mechanical stresses on the kinetics of ICT in silicon: (*a*, *b*) the overall overpotential and the stress modified surface overpotential at the charging rates of 1C and 3C, respectively and (*c*, *d*) comparison of voltage curves with and without considering the stress effect on the surface overpotential at 1C and 3C, respectively

electrode on the secondary and tertiary *y*-axes (right), respectively. The silicon active particle expands linearly with the lithium concentration and reaches a maximum of 235 % volumetric strain at the end of lithiation. This maximum strain is lower than the theoretical maximum expansion as the particle is not fully lithiated when the lower cut-off voltage of 0.1 V is reached. The expansion of the active particle is accommodated by (i) reduction in porosity, (ii) compaction of CBD, and (iii) expansion into the separator. Here, we are interested in the evolution of the porosity of the composite and thus its impact on the Li transport through the carbon network. Upon the completion of lithiation, the porosity drops by ~13.5 % from an initial value of 65.3 % in the model system. It is worth noting that the compaction of CBD is minimal compared to the reduction in porosity. The reduction in porosity directly impacts the transport of Li ions in the liquid electrolyte filled in the pore phase. This consequence is evident in the increase of tortuosity in Fig. 5(*a*). Changes in the microstructure are presented in a series of contour plots in Fig. 5(*b*), where we plot the normalized concentration distribution at various times during the lithiation process. Tortuosity change is most influential in the narrow gaps in CBD (highlighted by arrows in Fig. 5(*b*)). Further constriction of these gaps results in minimization of Li ion transport and the consequent depletion of Li ions at certain locations on the silicon surface. While we recognize that multiple transport pathways can be interconnected in actual three-dimensional microstructure, the 2D axisymmetric model provides an adequate representation of the impact of deformation on electrochemical transport, as most of the three-dimensional pathways are expected to be confined due to the massive deformation of the silicon particle.

First Cycle Capacity Loss by Asymmetric Diffusion Kinetics. The transport mechanism of Li in the solid active materials is strongly linked to the atomic structure of the host. Due to Li insertion, structural evolution in intercalating and alloying-type electrodes can alter the diffusion process. This change must be accounted for in modeling efforts in the form of changes in the diffusion coefficient with varying Li concentrations. This variation in diffusivity is observed experimentally for a wide range of electrode materials. We summarize the data from multiple studies for three

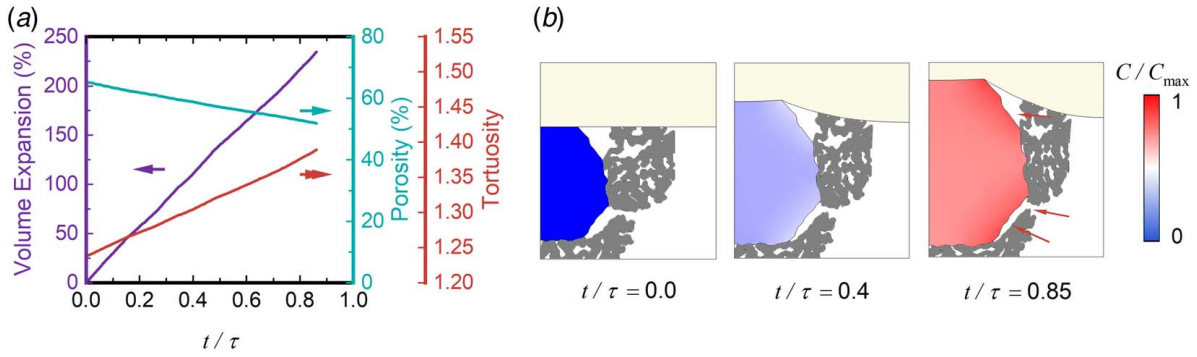

Fig. 5 Effect of mechanical deformation of the active particle on the microstructure of the porous electrode: (*a*) volume expansion of the silicon particle upon charging at 1C and the resulting reduction in cell porosity and increase in tortuosity and (*b*) Contour plots of normalized concentration C/C_{max} at the charging time $t/\tau = 0$, 0.4, and 0.85 depicting the volume expansion of silicon, compression of the separator, and consumption of porosity

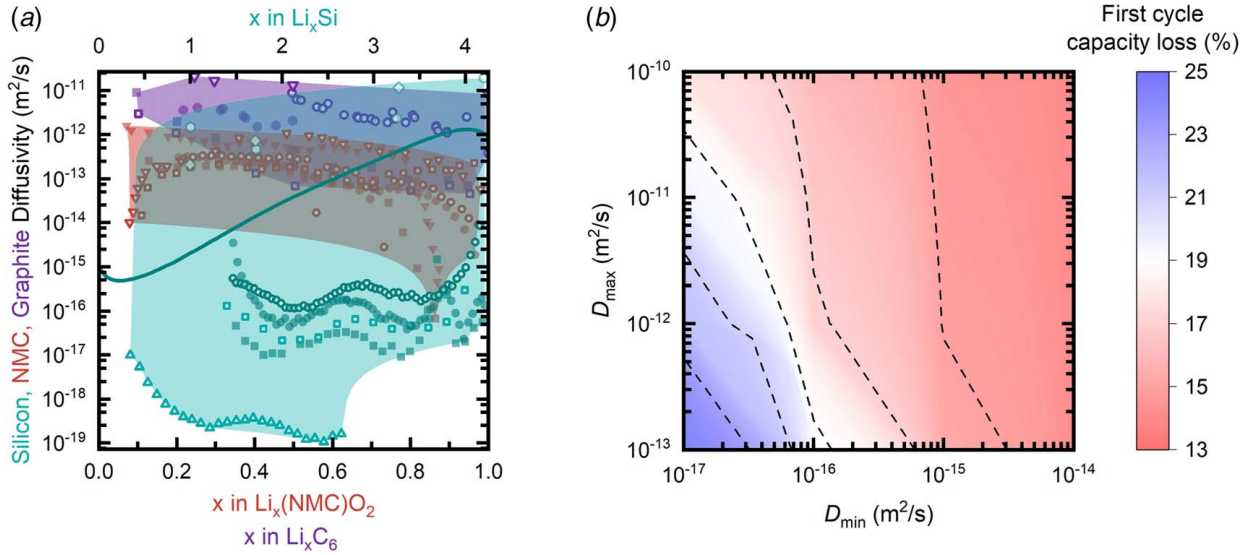

Fig. 6 First cycle capacity loss of the cell due to the SOC-dependent Li diffusivity and asymmetric rates for charging and discharging: (*a*) Concentration-dependent Li diffusion coefficient for NMC cathode, graphite anode, and silicon anode reported in literature and (*b*) A phase diagram of the first cycle capacity loss for a range of maximum and minimum Li diffusivities in silicon at the charging rate of 1C.

different materials: NMC [67–69], graphite [70–72], and silicon [73–76] in Fig. 6(*a*). While it is evident that diffusivity changes with varying Li content during charging and discharging for all three materials, the variation between different studies (marked by the shaded background) is substantial due to the disparities in the material composition and preparation, characterization techniques, and measurement conditions. Initial studies on the first cycle capacity loss of silicon electrodes were attributed to particle fracture and unstable SEI. Recent studies, however, have found that capacity loss occurs even in the absence of these effects [17,18]. de Vasconcelos et al. [20] showed that asymmetric diffusion kinetics during lithiation and delithiation leads to Li trapping within the particle and capacity loss. Given the considerable variation in measured diffusion coefficients and multiple methods available to tune the material diffusivity, we quantify the first cycle capacity loss for a set of maximum and minimum diffusion coefficients which were reported by literature. The solid teal line in Fig. 6(*a*) represents the base function (see Fig. S4 available in the Supplemental Materials on the ASME Digital Collection). used for the diffusivity of silicon [20] with $D_{min} = 10^{-15}$ m^2/s and $D_{max} = 10^{-12}$ m^2/s. The particle is charged and discharged at 1C. The diffusion coefficient, elastic modulus, and yield stress as functions of Li content are listed in Table 1. The phase diagram (Fig. 6(*b*)) presents the first cycle capacity loss using different diffusion coefficients, with D_{min} varying from 10^{-17} to 10^{-14} m^2/s and D_{max} varying from 10^{-13} to 10^{-10} m^2/s. The maximum and minimum capacity loss occurs when D_{max} and D_{min} are minimum and maximum, respectively, at a given charging rate. The capacity loss is dependent on both D_{max} and D_{min} when diffusivities are low. The dependence on D_{max} reduces at higher values of D_{min}, indicating that improving D_{min} alone can significantly improve the accessible capacity.

Conclusion

The computational study accurately captures multiple vital aspects of high-capacity composite electrodes in commercial batteries. The coupled electrochemomechanical model encapsulates the rate dependence of inelastic behavior of the active material and electrochemical response of the cell. The influence of intermolecular interaction within the active particle on the diffusion process is considered in the form of a concentration-dependent activity coefficient. We find that the thermodynamic non-ideality dominates the influence on diffusion over mechanical stresses and that an ideal solution assumption can drastically overestimate the stress effect. The equally important stress coupling with ICT reactions is investigated. We find it to be more significant in silicon than the cathode materials such as NMC due to the large amount of mechanical energy dissipation involved in the lithiation of silicon. Furthermore, we employ the microstructure resolved model to assess the impact of large volume expansion of silicon on the transport of Li ions in the liquid electrolyte-filled pore phase. We find that silicon expansion is accommodated partly by the separator compression and the consumption of porosity, leading to a considerable increase in the tortuosity of the conductive agent. Lastly, we model the underlying mechanism of Li trapping due to the asymmetric diffusion kinetics and quantify the resulting first cycle capacity loss due to the variation of the diffusion constants over several orders of magnitude. We provide a phase diagram as a guideline for material design to minimize the irreversible capacity lost due to Li trapping. By solving the comprehensive set of strongly coupled nonlinear governing equations, this computational tool opens a wide range of applications for accurately modeling the mechanical and electrochemical performance of high-capacity electrodes. Not only does it help to decode the depth of mechanoelectrochemical interactions, but it also presents a framework to model detailed microstructural evolution in the composite electrodes providing insight into the influence and consequence of the multiphysics and multi-phasic interactions.

Acknowledgment

The authors are grateful for the support from the National Science Foundation under Grant No. DMR-1832707.

Conflict of Interest

There are no conflicts of interest.

Data Availability Statement

The data sets generated and supporting the findings of this article are obtainable from the corresponding author upon reasonable request.

Appendix

Table 1 Computational parameters used in different scenarios of finite element modeling

Parameter	Value
Yield stress, σ_Y	
Independent of concentration C	1 GPa [77]
Concentration dependent	$-3.15(x/(1+x))+3$ GPa [20] where x is atomic fraction in Li_xSi
Elastic modulus, E	
Independent of concentration C	80 GPa [42]
Concentration dependent	$-80(C/C_{max})+120$ GPa [20]
Density of silicon, ρ	2230 kg/m^3
Viscoplastic material constants,	
A	0.0023 s^{-1} [40]
n	2.94 [40]
σ_{ref}	1 GPa
Conductivity of CBD, K_c	100 S/m [78]
Faraday constant, F	96485 C/mol
Universal gas constant, R	8.3145 J/(mol · K)
Absolute temperature, T	293.15 K
Anodic and cathodic transfer coefficients, α_a and α_c	0.5 [78]
Open-circuit potential, E_{eq}	Fig. S3 available in the Supplemental Materials on the ASME Digital Collection. [42]
Anodic and cathodic reaction rate constants, k_a and k_c	2×10^{-11} [47]
Maximum theoretical concentration of Li in silicon, C_{max}	3.6643×10^5 mol/m^3 [79]
Reference Li^+ concentration in electrolyte, C_{l_ref}	1 mol/m^3
Partial molar volume of Li in silicon, Ω	8.1872×10^{-6} m^3/mol [79]
Activity contribution in chemical potential, $RT\ln\gamma$	$\sum_{m=2}^{m}\Omega_m m\left(\frac{C}{C_{max}}\right)^{m-1}$ [42]
Ω_2/F	0.8735 V [42]
Ω_3/F	0.7185 V [42]
Ω_4/F	−4.504 V [42]
Ω_5/F	6.876 V [42]
Ω_6/F	−4.6272 V [42]
Ω_7/F	1.1744 V [42]
Diffusivity of Li in silicon, D	
Independent of concentration C	10^{-16} m^2/s [79]
Concentration dependent	Fig. S4 available in the Supplemental Materials on the ASME Digital Collection. [20]

References

[1] Chan, C. K., Peng, H., Liu, G., McIlwrath, K., Zhang, X. F., Huggins, R. A., and Cui, Y., 2008, "High-Performance Lithium Battery Anodes Using Silicon Nanowires," Nat. Nanotechnol., **3**(1), pp. 31–35.

[2] Graetz, J., Ahn, C. C., Yazami, R., and Fultz, B., 2004, "Nanocrystalline and Thin Film Germanium Electrodes With High Lithium Capacity and High Rate Capabilities," J. Electrochem. Soc., **151**(5), p. A698.

[3] Xu, Y., Liu, Q., Zhu, Y., Liu, Y., Langrock, A., Zachariah, M. R., and Wang, C., 2013, "Uniform Nano-Sn/C Composite Anodes for Lithium Ion Batteries," Nano Lett., **13**(2), pp. 470–474.

[4] Nitta, N., and Yushin, G., 2014, "High-Capacity Anode Materials for Lithium-Ion Batteries: Choice of Elements and Structures for Active Particles," Part. Part. Syst. Charact., **31**(3), pp. 317–336.

[5] Choi, J. W., and Aurbach, D., 2016, "Promise and Reality of Post-Lithium-Ion Batteries With High Energy Densities," Nat. Rev. Mater., **1**(4), p. 16013.

[6] Zhang, W.-J., 2011, "A Review of the Electrochemical Performance of Alloy Anodes for Lithium-Ion Batteries," J. Power Sources, **196**(1), pp. 13–24.

[7] Zhang, S., Zhao, K., Zhu, T., and Li, J., 2017, "Electrochemomechanical Degradation of High-Capacity Battery Electrode Materials," Prog. Mater. Sci., **89**, pp. 479–521.

[8] Beaulieu, L. Y., Eberman, K. W., Turner, R. L., Krause, L. J., and Dahna, J. R., 2001, "Colossal Reversible Volume Changes in Lithium Alloys," Electrochem. Solid-State Lett., **4**(9), pp. 7–10.

[9] Müller, S., Pietsch, P., Brandt, B. E., Baade, P., De Andrade, V., De Carlo, F., and Wood, V., 2018, "Quantification and Modeling of Mechanical Degradation in Lithium-Ion Batteries Based on Nanoscale Imaging," Nat. Commun., **9**(1), p. 2340.

[10] Chan, C. K., Ruffo, R., Hong, S. S., and Cui, Y., 2009, "Surface Chemistry and Morphology of the Solid Electrolyte Interphase on Silicon Nanowire Lithium-Ion Battery Anodes," J. Power Sources, **189**(2), pp. 1132–1140.

[11] Su, X., Wu, Q., Li, J., Xiao, X., Lott, A., Lu, W., Sheldon, B. W., and Wu, J., 2014, "Silicon-Based Nanomaterials for Lithium-Ion Batteries: A Review," Adv. Energy Mater., **4**(1), pp. 1–23 .

[12] Ulus, A., Electrochem, J., Soc, A., Ulus, A., Rosenberg, Y., Burstein, L., and Peled, E., 2002, "Tin Alloy-Graphite Composite Anode for Lithium-Ion Batteries Tin Alloy-Graphite Composite Anode for Lithium-Ion Batteries," J. Electrochem. Soc., **149**(5), p. A635.

[13] Radvanyi, E., Porcher, W., De Vito, E., Montani, A., Franger, S., and Larbi, S.J.S., 2014, "Failure Mechanisms of Nano-Silicon Anodes Upon Cycling: An Electrode Porosity Evolution Model," Phys. Chem. Chem. Phys., **16**(32), pp. 17142–17153.

[14] Pietsch, P., Westhoff, D., Feinauer, J., Eller, J., Marone, F., Stampanoni, M., Schmidt, V., and Wood, V., 2016, "Quantifying Microstructural Dynamics and Electrochemical Activity of Graphite and Silicon-Graphite Lithium Ion Battery Anodes," Nat. Commun., **7**(1), p. 12909.

[15] Dhillon, S., Hernández, G., Wagner, N. P., Mari, A., and Brandell, D., 2021, "Modelling Capacity Fade in Silicon-Graphite Composite Electrodes for Lithium-Ion Batteries," Electrochim. Acta, **377**, p. 138067.

[16] Jerliu, B., Hüger, E., Horisberger, M., Stahn, J., and Schmidt, H., 2017, "Irreversible Lithium Storage During Lithiation of Amorphous Silicon Thin Film Electrodes Studied by In-Situ Neutron Reflectometry," J. Power Sources, **359**, pp. 415–421.

[17] Lindgren, F., Rehnlund, D., Pan, R., Pettersson, J., Younesi, R., Xu, C., Gustafsson, T., Edström, K., and Nyholm, L., 2019, "On the Capacity Losses Seen for Optimized Nano-Si Composite Electrodes in Li-Metal Half-Cells," Adv. Energy Mater., **9**(33), p. 1901608.

[18] Rehnlund, D., Lindgren, F., Bo, S., Pettersson, J., Bexell, U., Boman, M., Edstro, K., and Nyholm, L., 2017, "Lithium Trapping in Alloy Forming Electrodes and Current Collectors for Lithium Based Batteries," Energy Environ. Sci., **10**(6), pp. 1350–1357.

[19] Zhu, B., Liu, G., Lv, G., Mu, Y., Zhao, Y., Wang, Y., and Li, X., 2019, "Minimized Lithium Trapping by Isovalent Isomorphism for High Initial Coulombic Efficiency of Silicon Anodes," Sci. Adv., **5**(11), p. eaax0651.

[20] de Vasconcelos, L. S., Xu, R., and Zhao, K., 2020, "Quantitative Spatiotemporal Li Profiling Using Nanoindentation," J. Mech. Phys. Solids, **144**, p. 104102.

[21] Nguyen, H. T., Yao, F., Zamfir, M. R., Biswas, C., So, K. P., Lee, Y. H., Kim, S. M., Cha, S. N., Kim, J. M., and Pribat, D., 2011, "Highly Interconnected Si Nanowires for Improved Stability Li-Ion Battery Anodes," Adv. Energy Mater., **1**(6), pp. 1154–1161.

[22] Chan, C. K., Zhang, X. F., and Cui, Y., 2008, "High Capacity Li Ion Battery Anodes Using Ge Nanowires," Nano Lett., **8**(1), pp. 307–309.

[23] Yao, Y., McDowell, M. T., Ryu, I., Wu, H., Liu, N., Hu, L., Nix, W. D., and Cui, Y., 2011, "Interconnected Silicon Hollow Nanospheres for Lithium-Ion Battery Anodes With Long Cycle Life," Nano Lett., **11**(7), pp. 2949–2954.

[24] Cui, G., Gu, L., Zhi, L., Kaskhedikar, N., Van Aken, P. A., Müllen, K., and Maier, J., 2008, "A Germanium-Carbon Nanocomposite Material for Lithium Batteries," Adv. Mater., **20**(16), pp. 3079–3083.

[25] Park, M.-H., Kim, M. G., Joo, J., Kim, K., Kim, J., Ahn, S., Cui, Y., and Cho, J., 2009, "Silicon Nanotube Battery Anodes," Nano Lett., **9**(11), pp. 3844–3847.

[26] Park, M. H., Cho, Y., Kim, K., Kim, J., Liu, M., and Cho, J., 2011, "Germanium Nanotubes Prepared by Using the Kirkendall Effect as Anodes for High-Rate Lithium Batteries," Angew. Chemie - Int. Ed., **50**(41), pp. 9647–9650.

[27] Liu, N., Wu, H., McDowell, M. T., Yao, Y., Wang, C., and Cui, Y., 2012, "A Yolk-Shell Design for Stabilized and Scalable Li-Ion Battery Alloy Anodes," Nano Lett., **12**(6), pp. 3315–3321.

[28] Zhang, W.-M., Hu, J.-S., Guo, Y.-G., Zheng, S.-F., Zhong, L.-S., Song, W.-G., and Wan, L.-J., 2008, "Tin-Nanoparticles Encapsulated in Elastic Hollow Carbon Spheres for High-Performance Anode Material in Lithium-Ion Batteries," Adv. Mater., **20**(6), pp. 1160–1165.

[29] Ko, M., Chae, S., Jeong, S., Oh, P., and Cho, J., 2014, "Elastic a-Silicon Nanoparticle Backboned Graphene Hybrid as a Self-Compacting Anode for High-Rate Lithium Ion Batteries," ACS Nano, **8**(8), pp. 8591–8599.

[30] Fan, Y., Zhang, Q., Xiao, Q., Wang, X., and Huang, K., 2013, "High Performance Lithium Ion Battery Anodes Based on Carbon Nanotube-Silicon Core-Shell Nanowires with Controlled Morphology," Carbon N. Y., **59**, pp. 264–269.

[31] Wang, X., Susantyoko, R. A., Fan, Y., Sun, L., Xiao, Q., and Zhang, Q., 2014, "Vertically Aligned CNT-Supported Thick Ge Films as High-Performance 3D Anodes for Lithium Ion Batteries," Small, **10**(14), pp. 2826–2829.

[32] Yi, R., Dai, F., Gordin, M., Chen, S., and Wang, D., 2013, "Micro-sized Si-C Composite With Interconnected Nanoscale Building Blocks as High-Performance Anodes.Pdf," Adv. Energy Mater., **3**(3), pp. 295–300.

[33] Tian, H., Tan, X., Xin, F., and Wang, C., 2015, "Micro-Sized Nano-Porous Si/C Anodes for Lithium Ion Batteries," Nano Energy, **11**, pp. 490–499.

[34] Dimov, N., Kugino, S., and Yoshio, M., 2004, "Mixed Silicon-Graphite Composites as Anode Material for Lithium Ion Batteries—Influence of Preparation Conditions on the Properties of the Material," J. Power Sources, **136**(1), pp. 108–114.

[35] Fuchsbichler, B., Stangl, C., Kren, H., Uhlig, F., and Koller, S., 2011, "High Capacity Graphite-Silicon Composite Anode Material for Lithium-Ion Batteries," J. Power Sources, **196**(5), pp. 2889–2892.

[36] Zheng, Y., Seifert, H. J., Shi, H., Zhang, Y., Kübel, C., and Pfleging, W., 2019, "3D Silicon/Graphite Composite Electrodes for High-Energy Lithium-Ion Batteries," Electrochim. Acta, **317**, pp. 502–508.

[37] Kim, H., Han, B., Choo, J., and Cho, J., 2008, "Three-Dimensional Porous Silicon Particles for Use in High-Performance Lithium Secondary Batteries," Angew. Chemie - Int. Ed., **47**(52), pp. 10151–10154.

[38] Ko, M., Chae, S., Ma, J., Kim, N., Lee, H. W., Cui, Y., and Cho, J., 2016, "Scalable Synthesis of Silicon-Nanolayer-Embedded Graphite for High-Energy Lithium-Ion Batteries," Nat. Energy, **1**(9), p. 16113.

[39] Xiao, Y., Cao, M., Ren, L., and Hu, C., 2012, "Hierarchically Porous Germanium-Modified Carbon Materials With Enhanced Lithium Storage Performance," Nanoscale, **4**(23), pp. 7469–7474.

[40] Pharr, M., Suo, Z., and Vlassak, J. J., 2014, "Variation of Stress With Charging Rate Due to Strain-Rate Sensitivity of Silicon Electrodes of Li-Ion Batteries," J. Power Sources, **270**, pp. 569–575.

[41] Verbrugge, M. W., and Koch, B. J., 1996, "Modeling Lithium Intercalation of Single-Fiber Carbon Microelectrodes," J. Electrochem. Soc., **143**(2), pp. 600–608.

[42] Bucci, G., Nadimpalli, S. P. V., Sethuraman, V. A., Bower, A. F., and Guduru, P. R., 2014, "Measurement and Modeling of the Mechanical and Electrochemical Response of Amorphous Si Thin Film Electrodes During Cyclic Lithiation," J. Mech. Phys. Solids, **62**(1), pp. 276–294.

[43] Sethuraman, V. A., Srinivasan, V., Bower, A. F., and Guduru, P. R., 2010, "In Situ Measurements of Stress-Potential Coupling in Lithiated Silicon," J. Electrochem. Soc., **157**(11), p. A1253.

[44] Bower, A. F., Guduru, P. R., and Sethuraman, V. A., 2011, "A Finite Strain Model of Stress, Diffusion, Plastic Flow, and Electrochemical Reactions in a Lithium-Ion Half-Cell," J. Mech. Phys. Solids, **59**(4), pp. 804–828.

[45] Lu, B., Song, Y., Zhang, Q., Pan, J., Cheng, Y. T., and Zhang, J., 2016, "Voltage Hysteresis of Lithium Ion Batteries Caused by Mechanical Stress," Phys. Chem. Chem. Phys., **18**(6), pp. 4721–4727.

[46] Ganser, M., Soc, J. E., Ganser, M., Hildebrand, F. E., Klinsmann, M., Hanauer, M., Kamlah, M., and Mcmeeking, R. M., 2019, "An Extended Formulation of Butler-Volmer Electrochemical Reaction Kinetics Including the Influence of Mechanics an Extended Formulation of Butler-Volmer Electrochemical Reaction Kinetics Including the Influence of Mechanics," J. Electrochem. Soc., **166**(4), pp. H167–H176.

[47] Xu, R., Yang, Y., Yin, F., Liu, P., Cloetens, P., Liu, Y., Lin, F., and Zhao, K., 2019, "Heterogeneous Damage in Li-Ion Batteries: Experimental Analysis and Theoretical Modeling," J. Mech. Phys. Solids, **129**, pp. 160–183.

[48] Liu, P., Xu, R., Liu, Y., Lin, F., and Zhao, K., 2020, "Computational Modeling of Heterogeneity of Stress, Charge, and Cyclic Damage in Composite Electrodes of Li-Ion Batteries," J. Electrochem. Soc., **167**(4), p. 040527.

[49] Xu, R., de Vasconcelos, L. S., and Zhao, K., 2016, "Computational Analysis of Chemomechanical Behaviors of Composite Electrodes in Li-Ion Batteries," J. Mater. Res., **31**(18), pp. 2715–2727.

[50] Smith, M., García, R. E., and Horn, Q. C., 2009, "The Effect of Microstructure on the Galvanostatic Discharge of Graphite Anode Electrodes in LiCoO2-Based Rocking-Chair Rechargeable Batteries," J. Electrochem. Soc., **156**(11), p. A896.

[51] Trembacki, B. L., Noble, D. R., Brunini, V. E., Ferraro, M. E., and Roberts, S. A., 2017, "Mesoscale Effective Property Simulations Incorporating Conductive Binder," J. Electrochem. Soc., **164**(11), pp. E3613–E3626.

[52] Trembacki, B. L., Mistry, A. N., Noble, D. R., Ferraro, M. E., Mukherjee, P. P., and Roberts, S. A., 2018, "Mesoscale Analysis of Conductive Binder Domain Morphology in Lithium-Ion Battery Electrodes," J. Electrochem. Soc., **165**(13), pp. E725–E736.

[53] Trembacki, B. L., Noble, D. R., Ferraro, M. E., and Roberts, S. A., 2020, "Mesoscale Effects of Composition and Calendering in Lithium-Ion Battery Composite Electrodes," ASME J. Electrochem. Energy Convers. Storage, **17**(4), p. 041001.

[54] Srivastava, I., Bolintineanu, D. S., Lechman, J. B., and Roberts, S. A., 2019, "Controlling Binder Adhesion to Impact Electrode Mesostructure and Transport," ACS Appl. Mater. Interfaces, **12**(31), pp. 34919–34930.

[55] Ferraro, M. E., Trembacki, B. L., Brunini, V. E., Noble, D. R., and Roberts, S. A., 2020, "Electrode Mesoscale as a Collection of Particles: Coupled Electrochemical and Mechanical Analysis of NMC Cathodes," J. Electrochem. Soc., **167**(1), p. 013543.

[56] Wang, M., Xiao, X., and Huang, X., 2017, "A Multiphysics Microstructure-Resolved Model for Silicon Anode Lithium-Ion Batteries," J. Power Sources, **348**, pp. 66–79.

[57] Gao, X., Lu, W., and Xu, J., 2020, "Modeling Framework for Multiphysics-Multiscale Behavior of Si–C Composite Anode," J. Power Sources, **449**, p. 227501.

[58] Liu, B., Jia, Y., Li, J., Jiang, H., Yin, S., and Xu, J., 2020, "Multiphysics Coupled Computational Model for Commercialized Si/Graphite Composite Anode," J. Power Sources, **450**, p. 227667.

[59] Fuller, T. F., Doyle, M., and Newman, J., 1994, "Simulation and Optimization of the Dual Lithium Ion Insertion Cell," J. Electrochem. Soc., **141**(1), pp. 1–10.

[60] Newman, J., and Thomas-Alyea, K. E., 2004, *Electrochemical Systems*, John Wiley and Sons, Hoboken, NJ.

[61] Hamann, C. H., Hamnett, A., and Vielstich, W., 2007, *Electrochemistry*, Wiley-VCH, Weinheim.

[62] Larché, F. C., and Cahn, J. W., 1985, "The Interactions of Composition and Stress in Crystalline Solids," Acta Metall., **33**(3), pp. 331–357.

[63] Drozdov, A. D., 2014, "Viscoplastic Response of Electrode Particles in Li-Ion Batteries Driven by Insertion of Lithium," Int. J. Solids Struct., **51**(3–4), pp. 690–705.

[64] de Vasconcelos, L. S., Xu, R., and Zhao, K., 2017, "Operando Nanoindentation: A New Platform to Measure the Mechanical Properties of Electrodes During Electrochemical Reactions," J. Electrochem. Soc., **164**(14), pp. A3840–A3847.

[65] Li, Y., Mao, W., Zhang, Q., Zhang, K., and Yang, F., 2020, "A Free Volume-Based Viscoplastic Model for Amorphous Silicon Electrode of Lithium-Ion Battery," J. Electrochem. Soc., **167**(4), p. 040518.

[66] Sheldon, B. W., Soni, S. K., Xiao, X., and Qi, Y., 2012, "Stress Contributions to Solution Thermodynamics in Li-Si Alloys," Electrochem. Solid-State Lett., **15**(1), pp. 9–12.

[67] Yang, S., Wang, X., Yang, X., Bai, Y., Liu, Z., Shu, H., and Wei, Q., 2012, "Determination of the Chemical Diffusion Coefficient of Lithium Ions in Spherical Li[Ni 0.5Mn 0.3Co 0.2]O 2," Electrochim. Acta, **66**, pp. 88–93.

[68] Zhou, H., Xin, F., Pei, B., and Whittingham, M. S., 2019, "What Limits the Capacity of Layered Oxide Cathodes in Lithium Batteries?," ACS Energy Lett., **4**(8), pp. 1902–1906.

[69] Hong, C., Leng, Q., Zhu, J., Zheng, S., He, H., Li, Y., Liu, R., Wan, J., and Yang, Y., 2020, "Revealing the Correlation Between Structural Evolution and Li + Diffusion Kinetics of Nickel-Rich Cathode Materials in Li-Ion Batteries," J. Mater. Chem. A, **8**(17), pp. 8540–8547.

[70] Pyun, S., and Ryu, Y. G., 1998, "Lithium Transport Through Graphite Electrodes That Contain Two Stage Phases," J. Power Sources, **70**(1), pp. 34–39.

[71] Persson, K., Sethuraman, V. A., Hardwick, L. J., Hinuma, Y., Meng, Y. S., Van Der Ven, A., Srinivasan, V., Kostecki, R., and Ceder, G., 2010, "Lithium Diffusion in Graphitic Carbon," J. Phys. Chem. Lett., **1**(8), pp. 1176–1180.

[72] Takami, N., Satoh, A., Hara, M., and Ohsaki, T., 1995, "Structural and Kinetic Characterization of Lithium Intercalation Into Carbon Anodes for Secondary Lithium Batteries," J. Electrochem. Soc., **142**(2), pp. 371–379.

[73] Ding, N., Xu, J., Yao, Y. X., Wegner, G., Fang, X., Chen, C. H., and Lieberwirth, I., 2009, "Determination of the Diffusion Coefficient of Lithium Ions in Nano-Si," Solid State Ionics, **180**(2–3), pp. 222–225.

[74] Wang, Z., Su, Q., Deng, H., and Fu, Y., 2015, "Composition Dependence of Lithium Diffusion in Lithium Silicide: A Density Functional Theory Study," ChemElectroChem, **2**(9), pp. 1292–1297.

[75] Huger, E., Dorrer, L., and Schmidt, H., 2018, "Permeation, Solubility, Diffusion and Segregation of Lithium in Amorphous Silicon Layers," Chem. Mater., **30**(10), pp. 3254–3264.

[76] Sivonxay, E., Aykol, M., and Persson, K. A., 2020, "The Lithiation Process and Li Diffusion in Amorphous SiO2 and Si From First-Principles," Electrochim. Acta, **331**, p. 135344.

[77] Mesgarnejad, A., and Karma, A., 2020, "Vulnerable Window of Yield Strength for Swelling-Driven Fracture of Phase-Transforming Battery Materials," NPJ Comput. Mater., **6**(1), p. 58.

[78] Smith, K., and Wang, C. Y., 2006, "Solid-State Diffusion Limitations on Pulse Operation of a Lithium Ion Cell for Hybrid Electric Vehicles," J. Power Sources, **161**(1), pp. 628–639.

[79] Xu, R., and Zhao, K., 2016, "Mechanical Interactions Regulated Kinetics and Morphology of Composite Electrodes in Li-Ion Batteries," Extrem. Mech. Lett., **8**, pp. 13–21.